3D Imaging and Manipulation of Subsurface Selenium Vacancies in $PdSe_2$

Giang D. Nguyen,[1] Liangbo Liang,[1,*] Qiang Zou,[1] Mingming Fu,[1] Akinola D. Oyedele,[1,2] Bobby G. Sumpter,[1,3] Zheng Liu,[4] Zheng Gai,[1] Kai Xiao,[1] and An-Ping Li[1,†]

[1]*Center for Nanophase Materials Sciences, Oak Ridge National Laboratory, Oak Ridge, Tennessee 37831, USA*
[2]*Bredesen Center for Interdisciplinary Research and Graduate Education, University of Tennessee, Knoxville, Tennessee 37996, USA*
[3]*Oak Ridge National Laboratory, Computational Sciences and Engineering Division, Oak Ridge, Tennessee 37831, USA*
[4]*Center for Programmable Materials, School of Materials Science and Engineering, Nanyang Technological University, Singapore 639798, Singapore*

(Received 23 April 2018; published 20 August 2018)

Two-dimensional materials such as layered transition-metal dichalcogenides (TMDs) are ideal platforms for studying defect behaviors, an essential step towards defect engineering for novel material functions. Here, we image the 3D lattice locations of selenium-vacancy V_{Se} defects and manipulate them using a scanning tunneling microscope (STM) near the surface of $PdSe_2$, a recently discovered pentagonal layered TMD. The V_{Se} show a characterisitc charging ring in a spatially resolved conductance map, based on which we can determine its subsurface lattice location precisely. Using the STM tip, not only can we reversibly switch the defect states between charge neutral and charge negative, but also trigger migrations of V_{Se} defects. This allows a demonstration of direct "writing" and "erasing" of atomic defects and tracing the diffusion pathways. First-principles calculations reveal a small diffusion barrier of V_{Se} in $PdSe_2$, which is much lower than S vacancy in MoS_2 or an O vacancy in TiO_2. This finding opens an opportunity of defect engineering in $PdSe_2$ for such as controlled phase transformations and resistive-switching memory device application.

DOI: 10.1103/PhysRevLett.121.086101

Vacancy defects play a significant role in determining the physical properties of crystalline materials. Most notably, a charge neutral vacancy (V^0) can capture an electron (V^-) or emit an electron (V^+) to become charge states, and each of these states will introduce a different type of dopant in semiconductors. Understanding vacancy behaviors constitutes a significant step in defect engineering that not only modifies the conductance of semiconductors, but also enables novel material functions ranging from high-spin states, such as nitrogen-vacancy centers in diamond [1], ionic diffusion paths enabled by oxygen vacancies in perovskite [2], and catalytic sites introduced by sulfur vacancies in MoS_2 [3]. Therefore, controlling vacancy defects, especially the ability of reverably manipulating vacancies at the atomic level, has become a promising approach to defect engineering and novel material functions [4–8]. As an example, Yang *et al.* demonstrated a memristor operation by controlling the migration of oxygen vacancy in TiO_2 under an applied electric field, but the precision of control was limited to the size of the device on a 50 nm scale [2]. Using a scanning tunneling microscope (STM) tip, Setvín *et al.* were able to pull oxygen vacancies to the surface with a high bias voltage (~5 V) to alter the surface properties of TiO_2 [9], but a reverable process remains to be demonstrated. Recently, the advent of 2D materials have attracted great research interest on vacancy defects in graphene and transition-metal dichalcogenites (TMDs) [3,10,11]. For example, Sangwan *et al.* reported a gate-tunable memristive behavior based on control of defect migration at the grain boundary in MoS_2 [12]. However, there has been no report on atomic control of the vacancy diffusion process in 2D materials.

$PdSe_2$, a newly discovered pentagonal TMD [13–16], has recently attracted vibrant research interest due to the extraordinary high carrier mobility [13] and air stability [15], which are desirable for 2D electronic applications. In contrast to the frequently reported hexagonal phases in layered TMDs, $PdSe_2$ has an uncommon pentagonal network with a puckered lattice structure. Each $PdSe_2$ slab consists of a Se-Pd-Se trilayer, where each Pd atom is bonded to four Se atoms located on the top and bottom sublayers [15], as illustrated in Fig. 1(a). The two Se atoms located in the top and bottom sublayers form a tilted Se-Se dumbbell crossing the Pd layer, resulting in a lack of rotational symmetry. Such structure is potentially sensitive to defects, as Se vacancy V_{Se} would break the symmetry of the Se-Se dumbbell and induce large structural distortion [14]. This contrasts with the commonly observed layered hexagonal TMDs, where the lattice remains intact even at a relatively high concentration of chalcogen vacancy [17].

In this Letter, we report on imaging and manipulation of individual Se vacancies V_{Se} in $PdSe_2$ using a STM. By imaging the characteristic charge rings of defects arising from a tip-induced band bending (TIBB) effect

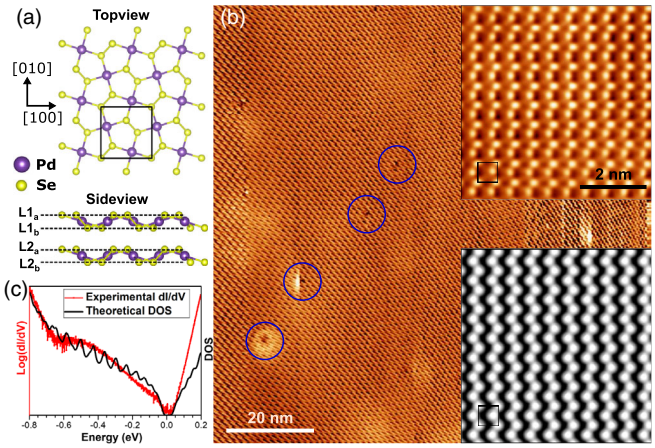

FIG. 1. Probing the structure and band gap on $PdSe_2$ surface. (a) Sketch of the crystallographic structure of $PdSe_2$ with the purple and yellow spheres representing the Pd and Se atoms, respectively. $L1_a, L1_b, ...$, define Se sublayers along the [001] direction where the Se top surface layer is counted as layer $L1_a$. (b) A typical STM topographic image of $PdSe_2$, blue circles indicate some V_{Se} defects (sample bias $V_s = -1.0$ V, tunneling current $I = 50$ pA, temperature $T = 120$ K). The inset in (b) shows the atomically resolved STM image (top right corner, Fourier filtering was applied to enhance the contrast) and simulated image (bottom right corner) of $PdSe_2$ at 0.3 V. (c) dI/dV spectrum on $PdSe_2$ in comparison with theoretical DOS of $PdSe_2$ ($V_s = -0.9$ V, $I = 3$ nA, $V_{ac} = 10$ mV, $f = 1000$ Hz, $T = 120$ K).

[4–8,18–22], we first determine the 3D lattice locations of V_{Se} precisely in the subsurface region. We then demonstrate the use of a STM tip as a movable electrostatic gate to manipulate V_{Se} by reversibly switching the charge states of defects between neutral V^0 and negative V^- states. We find a relatively small bias voltage (~2.0 V) at the STM tip can be used to trigger vacancy migrations, which allows us to demonstrate both direct writing and erasing of atomic defects in $PdSe_2$ while tracing their diffusion pathways. The results are corroborated by first-principles calculations that reveal the formation energies and diffusion barriers of Se vacancies in $PdSe_2$. This work opens an opportunity for defect engineering in $PdSe_2$ at the atomic level to achieve controlled phase transformations [14,23] or new material functions such as resistive-switching memory [12,24–27].

Here, we study the behaviors of individual defects by visualizing and manipulating V_{Se} in bulk $PdSe_2$ with a STM. $PdSe_2$ single crystals were synthesized by a self-flux method as previously reported [15]. A bulk crystal of $PdSe_2$ was cleaved along the [001] direction *in situ* in ultrahigh vacuum at room temperature. Figure 1(b) shows a typical STM image of a cleaved $PdSe_2$ surface. The atomically resolved STM image [upper inset of Fig. 1(b)] shows a square network with lattice constants of 0.58 ± 0.01 nm and bright spots visualizing the Se atoms on the topmost sublayer. A simulated image [lower inset of Fig. 1(b)] is in excellent agreement with the STM image, corroborating this interpretation. $PdSe_2$ has an orthorhombic unit cell with in-plane lattice constants of $a \approx 0.575$ nm and $b \approx 0.587$ nm [28], and its in-plane unit cell is very close to the square network shown in Fig. 1(b) after considering experimental uncertainty. Figure 1(c) shows the measured dI/dV spectrum (red curve) with a band gap of 0.06 ± 0.02 eV (see Supplemental Material, Fig. S1 for more details [29], with Refs. [30–32]). This measured band gap is corroborated by calculated density of states (DOS) [black curve in Fig. 1(c)] using density-functional theory with the many-body GW approximation. Individual V_{Se} defects on $PdSe_2$ can be visualized by STM images. Defects on the top surface are shown as dark holes, which indicates the missing of Se surface atoms [blue circles in Fig. 1(b)]. This observation confirms the existence of V_{Se} in $PdSe_2$ as reported previously [14]. The V_{Se} introduces unoccupied in-gap states (Fig. S2), which can be revealed as alternative dark and bright contrast when varying sample bias from positive to negative values (see Fig. S3 for more details [29]).

We now examine V_{Se} defect behaviors. Figure 2(a) shows a STM topographic image on an area with 11 V_{Se} defects labeled numerically. In the spatially resolved differential conductance dI/dV maps [Figs. 2(b)–2(f)], these defects appear as a ringlike feature in the sample bias range of 0.9–0.4 V. At a constant bias voltage below

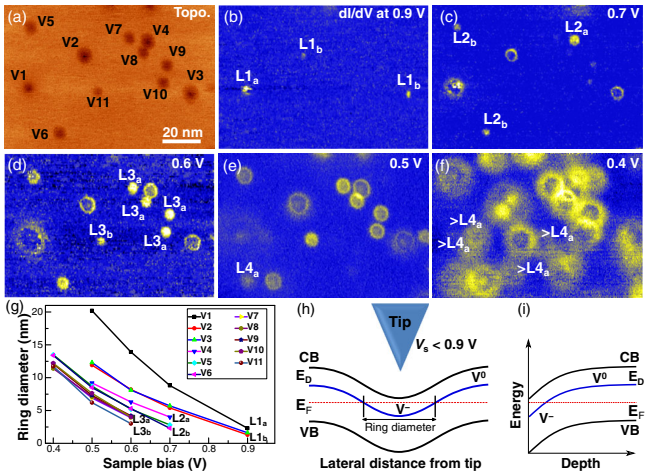

FIG. 2. Imaging Se-vacancy defects and switching charge state of the defects in $PdSe_2$. (a) STM topographic image showing V_{Se} defects as dark disks and labeled as $V1$ to $V11$ ($V_s = 0.5$ V, $I = 50$ pA, $T = 120$ K). (b)–(f) The evolution of measured differential conductance dI/dV map as a function of sample bias, showing defects located on different lattice layers as rings of different diameters. (g) The dependence of ring diameter as a function of sample bias for 11 defects. (h) A sketch of the lateral tip-induced band bending on the sample below the STM tip showing the switch of charge neutral V^0 to negative state V^-. (i) A sketch of depth-dependent band bending of conduction band (CB), valence band (VB), and defect state (E_D) below the tip position.

the threshold, a higher tunneling current leads to a larger ring (Fig. S4 [29]). This result indicates that the ring size actually varies with the tip-sample distance in which a farther separation results in a smaller ring [Fig. S4(f)]. These observations suggest that the ring features in dI/dV maps do not correlate with the local DOS; instead, they can be explained as defect charge states due to the TIBB effect [33]. Similar features were previously observed in doped semiconductors GaAs [34] and InAs [18], Co-adatoms in graphene [35], vacancies in black phosphorous [22], and Fe dopants in Bi_2Se_3 [36]. The switch of charge state gives rise to the ring feature in dI/dV maps, which occurs at a specific voltage when the dopant level crosses the bulk Fermi level [Fig. 2(h)] [18,22,34]. In such a process, larger rings are expected for a smaller sample bias and smaller tip-sample separation (larger TIBB). Therefore, depending on the sample bias, the STM tip can switch reversibly the charge states of an individual V_{Se} defect in $PdSe_2$ between V^0 and V^- (Fig. S5 [29]).

Figure 2(g) shows the change of ring diameter as a function of the sample bias voltage for the 11 defects labeled in Fig. 2(a). The charging rings become smaller as bias voltage approaches the threshold, corroborating a TIBB process. At the same bias voltage, different ring sizes indicate the different depths of these defects from the surface of $PdSe_2$. The defects located at a deeper layer have smaller TIBB [Fig. 2(i)], and thus their rings are smaller. Moreover, defects deeper below the surface have a lower charging threshold, which is clearly seen in the dI/dV maps shown in Figs. 2(b)–2(f). Based on this information, we can assign V_{Se} defects to individual Se sublayers, as shown in Figs. 2(b)–2(g), although the assignment for deeper than the third layer ($L3$) is less accurate due to the limit of statistical data. The onset voltage of charging ring of defects in the two sublayers of the same $PdSe_2$ slab is almost the same, e.g., 0.9 V for $L1_a$ and $L1_b$, 0.7 V for $L2_a$ and $L2_b$, and 0.6 V for $L3_a$ and $L3_b$. This is simply because the distance between two Se sublayers in one $PdSe_2$ slab is smaller compared to the distance between two adjacent Se sublayers at two $PdSe_2$ slabs [15]. Therefore, the STM tip not only allows us to reversibly switch the charge state of a V_{Se} defect, but also enables us to identify the location of the defects in the subsurface atomic lattice. It provides us a capability for precise 3D imaging of individual defects in a crystalline lattice, especially in 2D layered materials where their atomic layers are well separated.

We now try to manipulate V_{Se} by changing its lattice locations with the STM tip. Figure 3(a) shows three V_{Se} located, respectively, on lattice layers $L1_b$, $L2_b$, and $L3_a$ according to the sizes of their charge rings and voltage thresholds (the complete set of dI/dV maps at different biases is shown in Fig. S6). A new V_{Se} defect emerges on layer $L2_a$, as shown in Fig. 3(b), after scanning the area with a high negative sample bias (-1 V with a tunneling current of 50 pA). We believe that the STM tip at negative

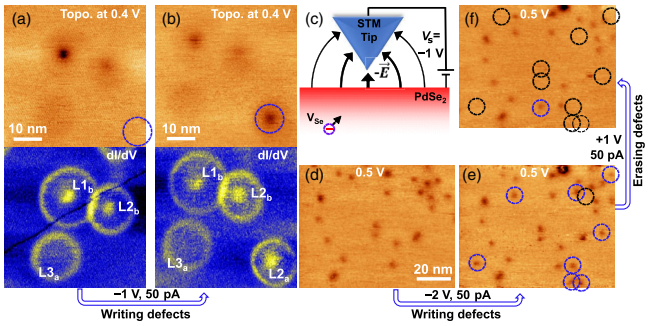

FIG. 3. Manipulation of Se-vacancy defects by a STM tip. (a),(b) STM topographic images (upper) and dI/dV maps (lower) before (a) and after (b) treating the sample area with a STM tip by scanning at $V_s = -1.0$ V, $I = 50$ pA. The images and dI/dV maps are acquired at $V_s = 0.4$ V, $I = 50$ pA, $V_{ac} = 50$ mV, $f = 1000$ Hz, $T = 120$ K. (c) Schematic illustrating V_{Se} migration to underneath the STM tip induced by the electrical field from the STM tip. (d)–(f) V_{Se} defects induced and removed on the surface after treating the surface by scanning at -2 and $+1$ V, respectively. The images are acquired at $V_s = 0.5$ V, $I = 50$ pA, $T = 120$ K. Blue dashed circles mark the new defects; black circles indicate defect disappearance.

sample bias triggers V_{Se} migration to underneath the tip during scanning, as illustrated in Fig. 3(c). This hypothesis is corroborated with a controlled experiment. Figure 3(d) is a STM image acquired at a normal condition of $V_s = 0.5$ V, $I = 50$ pA, showing V_{Se} defects as dark spots. The same area of the $PdSe_2$ surface is then treated by STM scanning with a high negative bias at -2 V, 50 pA. Figure 3(e) is then acquired with the normal condition, which contains new V_{Se} defects in the sample area, as marked by dashed blue circles. Most of these defects disappear after a reverse treatment with a high positive sample bias (1 V, 50 pA), as marked by dashed black circles in Fig. 3(f). This kind of tip-induced vacancy "writing and erasing" process is similar to that observed recently in oxygen vacancies V_O in TiO_2 [9,37], although a significantly higher bias (5.2 V) was required for moving V_O and only the writing process was demonstrated in TiO_2 with the STM tip. It is noted that the field-induced migration of V_O in metal oxides is already applied in novel resistive memory device applications [2,27]. Our result shows that 2D materials like $PdSe_2$ can be next generation materials for the memory device with much lower energy consumption and higher efficiency.

To understand the tip-induced V_{Se} migration in $PdSe_2$, we calculated the energy barriers for V_{Se} diffusion between two layers (interlayer) or within the same layer (intralayer) using the climbing image nudged elastic band method [38]. The nudged elastic band method finds saddle points and minimum energy paths between the initial and final states, by optimizing a number of intermediate images along the reaction path (see more details in the Supplemental Material [29], with additional Refs. [38–43]). The four possible configurations for V_{Se} positions (marked with red

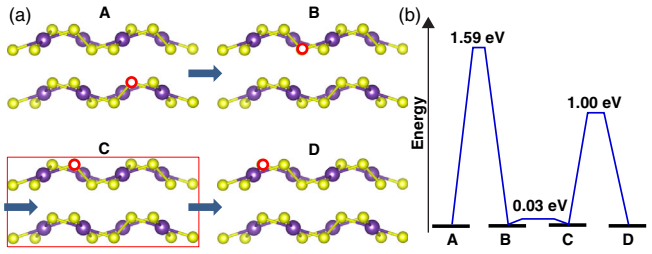

FIG. 4. Se-vacancy diffusion between two layers or within the same layer. (a) Schematic of different V_{Se} configurations in the $PdSe_2$ sample, with the red circle marking the V_{Se} site. (b) Calculated energy barriers for V_{Se} diffusion between the different defect configurations.

circles) are sketched and labeled as *A*, *B*, *C*, and *D* in Fig. 4(a). The corresponding energy barriers for the diffusion of a V_{Se} between these configurations are shown in Fig. 4(b). The relaxed atomic structures for these four configurations and the corresponding transition states are shown in Fig. S7 [29]. The energy barrier is 1.59 eV for the interlayer V_{Se} diffusion from configuration *A* to *B*. In comparison, we performed a similar calculation for S vacancy V_S in MoS_2 and find a much higher barrier of 4.44 eV for the similar interlayer V_{Se} diffusion in MoS_2. This significant difference can be attributed to the fact that the interlayer binding energy in $PdSe_2$ is notably larger than that in MoS_2, and the average interlayer distance in $PdSe_2$ is much shorter than that in MoS_2 [15,44,45]. Furthermore, for the intralayer V_{Se} diffusion in $PdSe_2$ from configuration *C* to *D*, the energy barrier is computed to be around 1 eV, which is also much lower than the barrier (2.30 eV) for the corresponding intralayer V_S diffusion in MoS_2 [46]. Compared to hexagonal MoS_2, the unique pentagonal network with relatively weaker covalent bond strength in $PdSe_2$ facilitates the V_{Se} migration. Finally, almost no barrier (0.03 eV) exists for the intralayer V_{Se} diffusion from configuration *B* to *C*, i.e., from the bottom Se sublayer to the top Se sublayer [Fig. 4(a)], due to the covalent bond between these two Se atoms (also see Fig. S7 [29]). In short, unlike the well-known MoS_2, the V_{Se} diffusion in $PdSe_2$ is considerably easier. This is consistent with an additional experiment where we find that V_{Se} can easily diffuse both vertically and laterally in the $PdSe_2$ at room temperature, even when scanning at relatively low sample bias of 0.4 V (Fig. S8). Thus, a STM tip can be used both to trigger vacancy migration and to trace the pathways of vacancy diffusion. However, in our experiment, we often observed the diffusion of a Se vacancy in about 10 nm. It must consist of multiple movement steps.

In conclusion, we have shown how a STM can be used for 3D imaging and manipulation of individual V_{Se} defects in $PdSe_2$. The V_{Se} is shown as a circular ring feature in a spatially resolved conductance map whose diameter changes in response to a TIBB effect. Based on the behaviors of this charging ring, the subsurface lattice location of V_{Se} can be precisely determined. The TIBB can be further utilized to reversibly switch the defect from charge neutral to charge negative states. Moreover, the electrical field from a STM tip can induce migrations of vacancies, which allows direct writing and erasing of atomic defects and tracing the diffusion pathways of V_{Se}. The diffusion kinetic barrier of V_{Se} in $PdSe_2$ is much lower than V_O in TiO_2 or V_S in MoS_2, paving the way for manipulating the V_{Se} in $PdSe_2$ in defect engineering for novel functionalities, such as controlled phase transformations [14,23] and memory device application [12,24–27].

This research was conducted at the Center for Nanophase Materials Sciences, which is a DOE Office of Science User Facility. L. L. was supported by the Eugene P. Wigner Fellowship at the Oak Ridge National Laboratory (ORNL). Part of the computations were performed using the resources of the Center for Computational Innovation at Rensselaer Polytechnic Institute.

*Corresponding author.
liangl1@ornl.gov
†Corresponding author.
apli@ornl.gov

[1] L. Childress, M. G. Dutt, J. Taylor, A. Zibrov, F. Jelezko, J. Wrachtrup, P. Hemmer, and M. Lukin, Science **314**, 281 (2006).
[2] J. J. Yang, M. D. Pickett, X. Li, D. A. Ohlberg, D. R. Stewart, and R. S. Williams, Nat. Nanotechnol. **3**, 429 (2008).
[3] D. Le, T. B. Rawal, and T. S. Rahman, J. Phys. Chem. C **118**, 5346 (2014).
[4] D. Eom, E. Seo, and J.-Y. Koo, Phys. Rev. B **94**, 195308 (2016).
[5] D.-H. Lee and J. A. Gupta, Nano Lett. **11**, 2004 (2011).
[6] H. Liu, H. Zheng, F. Yang, L. Jiao, J. Chen, W. Ho, C. Gao, J. Jia, and M. Xie, ACS Nano **9**, 6619 (2015).
[7] J. Riffle, C. Flynn, B. St. Laurent, C. Ayotte, C. Caputo, and S. Hollen, J. Appl. Phys. **123**, 044301 (2018).
[8] H. Zheng, A. Weismann, and R. Berndt, Phys. Rev. Lett. **110**, 226101 (2013).
[9] M. Setvín, U. Aschauer, P. Scheiber, Y.-F. Li, W. Hou, M. Schmid, A. Selloni, and U. Diebold, Science **341**, 988 (2013).
[10] S. M. Hus and A.-P. Li, Prog. Surf. Sci. **92**, 176 (2017).
[11] S. Zhang, C.-G. Wang, M.-Y. Li, D. Huang, L.-J. Li, W. Ji, and S. Wu, Phys. Rev. Lett. **119**, 046101 (2017).
[12] V. K. Sangwan, D. Jariwala, I. S. Kim, K.-S. Chen, T. J. Marks, L. J. Lauhon, and M. C. Hersam, Nat. Nanotechnol. **10**, 403 (2015).
[13] W. L. Chow *et al.*, Adv. Mater. **29**, 1602969 (2017).
[14] J. Lin, S. Zuluaga, P. Yu, Z. Liu, S. T. Pantelides, and K. Suenaga, Phys. Rev. Lett. **119**, 016101 (2017).
[15] A. D. Oyedele *et al.*, J. Am. Chem. Soc. **139**, 14090 (2017).
[16] M. A. ElGhazali, P. G. Naumov, H. Mirhosseini, V. Süß, L. Müchler, W. Schnelle, C. Felser, and S. A. Medvedev, Phys. Rev. B **96**, 060509 (2017).
[17] M. Mahjouri-Samani *et al.*, Nano Lett. **16**, 5213 (2016).

[18] F. Marczinowski, J. Wiebe, J.-M. Tang, M. E. Flatté, F. Meier, M. Morgenstern, and R. Wiesendanger, Phys. Rev. Lett. **99**, 157202 (2007).
[19] F. Marczinowski, J. Wiebe, F. Meier, K. Hashimoto, and R. Wiesendanger, Phys. Rev. B **77**, 115318 (2008).
[20] N. A. Pradhan, N. Liu, C. Silien, and W. Ho, Phys. Rev. Lett. **94**, 076801 (2005).
[21] A. P. Wijnheijmer, J. K. Garleff, K. Teichmann, M. Wenderoth, S. Loth, R. G. Ulbrich, P. A. Maksym, M. Roy, and P. M. Koenraad, Phys. Rev. Lett. **102**, 166101 (2009).
[22] Z. Qiu *et al.*, Nano Lett. **17**, 6935 (2017).
[23] S. Bordier, A. Chocard, and S. Gossé, J. Nucl. Mater. **451**, 120 (2014).
[24] H.-S. P. Wong, H.-Y. Lee, S. Yu, Y.-S. Chen, Y. Wu, P.-S. Chen, B. Lee, F. T. Chen, and M.-J. Tsai, Proc. IEEE **100**, 1951 (2012).
[25] R. Ge, X. Wu, M. Kim, J. Shi, S. Sonde, L. Tao, Y. Zhang, J. C. Lee, and D. Akinwande, Nano Lett. **18**, 434 (2018).
[26] V. K. Sangwan, H.-S. Lee, and M. C. Hersam, in *Electron Devices Meeting (IEDM), 2017 IEEE International* (IEEE, New York, 2017), p. 5.
[27] A. Sawa, Mater. Today **11**, 28 (2008).
[28] C. Soulard, X. Rocquefelte, P.-E. Petit, M. Evain, S. Jobic, J.-P. Itie, P. Munsch, H.-J. Koo, and M.-H. Whangbo, Inorg. Chem. **43**, 1943 (2004).
[29] See Supplemental Material at http://link.aps.org/supplemental/10.1103/PhysRevLett.121.086101 for detailed methods on theoretical calculations and additional data, which includes Refs. [30–32].
[30] C. Domke, P. Ebert, and K. Urban, Surf. Sci. **415**, 285 (1998).
[31] S. Haldar, H. Vovusha, M. K. Yadav, O. Eriksson, and B. Sanyal, Phys. Rev. B **92**, 235408 (2015).
[32] S. Loth, M. Wenderoth, K. Teichmann, and R. Ulbrich, Solid State Commun. **145**, 551 (2008).
[33] R. M. Feenstra and J. A. Stroscio, J. Vac. Sci. Technol. B **5**, 923 (1987).
[34] K. Teichmann, M. Wenderoth, S. Loth, R. G. Ulbrich, J. K. Garleff, A. P. Wijnheijmer, and P. M. Koenraad, Phys. Rev. Lett. **101**, 076103 (2008).
[35] V. W. Brar *et al.*, Nat. Phys. **7**, 43 (2011).
[36] C.-L. Song, Y.-P. Jiang, Y.-L. Wang, Z. Li, L. Wang, K. He, X. Chen, X.-C. Ma, and Q.-K. Xue, Phys. Rev. B **86**, 045441 (2012).
[37] S. Selçuk and A. Selloni, J. Chem. Phys. **141**, 084705 (2014).
[38] G. Henkelman, B. P. Uberuaga, and H. Jónsson, J. Chem. Phys. **113**, 9901 (2000).
[39] M. Dion, H. Rydberg, E. Schröder, D. C. Langreth, and B. I. Lundqvist, Phys. Rev. Lett. **92**, 246401 (2004).
[40] G. Kresse and J. Furthmüller, Comput. Mater. Sci. **6**, 15 (1996).
[41] A. A. Mostofi, J. R. Yates, G. Pizzi, Y.-S. Lee, I. Souza, D. Vanderbilt, and N. Marzari, Comput. Phys. Commun. **185**, 2309 (2014).
[42] J. P. Perdew, K. Burke, and M. Ernzerhof, Phys. Rev. Lett. **77**, 3865 (1996).
[43] http://theory.cm.utexas.edu/vtsttools/neb.html.
[44] J. Sun, H. Shi, T. Siegrist, and D. J. Singh, Appl. Phys. Lett. **107**, 153902 (2015).
[45] T. Björkman, A. Gulans, A. V. Krasheninnikov, and R. M. Nieminen, Phys. Rev. Lett. **108**, 235502 (2012).
[46] H.-P. Komsa, S. Kurasch, O. Lehtinen, U. Kaiser, and A. V. Krasheninnikov, Phys. Rev. B **88**, 035301 (2013).